RSC Advances




ROYAL SOCIETY OF CHEMISTRY

www.rsc.org/advances

# Improved photocatalytic activity of $MoS_2$ nanosheets decorated with $SnO_2$ nanoparticles

**S.V. Prabhakar Vattikuti[1*], Chan Byon[1*], Ch. Venkata Reddy[1] and R.V.S.S.N.Ravikumar[2]**

[1]School of Mechanical Engineering, Yeungnam University, Gyeongsan, South Korea, 712-749
[2]Department of Physics, Acharya Nagarjuna University, A.P, India, 522510

* Corresponding Authors/ E-mail: vsvprabu@gmail.com, and cbyon@ynu.ac.kr
TEL: +82-10-4017-8527, FAX: +82-53-810-4627

## Abstract

$MoS_2$ nanosheet decorated with $SnO_2$ mesoporous nanoparticles were successfully prepared by a facile two-step method. $MoS_2$ nanosheets were pre-synthesized using a solvothermal method and then decorated with the $SnO_2$ mesoporous nanoparticles through a wet chemical method. The nanocomposite was characterized with powder X-ray diffraction (XRD), field emission scanning electron microscopy (FESEM), energy dispersed spectrometry (EDX), high-resolution transmission electron microscopy (HRTEM), thermal gravimetric and differential thermal analysis (TG-DTA), X-ray photoelectron spectroscopy (XPS) and Electrochemcial impedance spectroscopy (EIS). $SnO_2$ mesoporous nanoparticles can be selectively formed and attached to the peripheral surface of the layered $MoS_2$, which was confirmed by FESEM and HRTEM. The photocatalytic activity of the nanocomposite was examined with Rhodamine B (RhB) in aqueous solution under UV light irradiation. The $SnO_2$ nanoparticles remarkably suppressed the electron-hole recombination effect on the $MoS_2$ photocatalyst and improved photocatalytic activity compared to pristine $MoS_2$ catalyst. A higher rate of pollutant degradation was accomplished within 50 min that was three times higher than that of the pristine $MoS_2$ catalyst.

**Keywords:** Nanocomposite, Photocatalyst, Solvothermal, Wet chemical Method, $MoS_2$

## Introduction

Molybdenum disulfide ($MoS_2$) can be made into a type of layered structure material similar to graphene. $MoS_2$ has hexagonally packed crystals comprising two of S-Mo-S tri-layers that are weakly bonded by van der Waals interaction [1, 2]. The S-Mo-S tri-layer consists of terrace sites on the basal plane and edge sites at the edges of nanoparticles [3]. Catalytically active edge sites of $MoS_2$ are difficult to understand and use for advanced catalyst design and developing improved catalytic materials [3], and effective synthesis of $MoS_2$ with well-

defined edge sites has been challenging and rarely reported.

$MoS_2$ is used as a solid lubricant and a catalyst for petroleum purification [4, 5]. It has been gaining increasing attention in the semiconductor industry due to its unique properties. In particular, different morphological forms of $MoS_2$ have attracted a recent surge of attention due to their morphology-dependent properties. Such forms include nanotubes [6], nanorods [7, 8], nanosheets [9], nanospheres [4, 10], single-layer structures, and multi-layer structures [11]. These forms can be suitable for application to solar cells [12], nanoelectronics [13], optoelectronics [14], tribology [4], and catalysis [5]. Monolayer $MoS_2$ could possibly be produced reliably by mechanical exfoliation [15] or chemically from the bulk material [16]. The development of heterostructure devices has gained scientific interest for emerging applications, such as controlled photoluminescence, photocatalysts, plasmonic devices, and sensors [17-19]. Nanointerfacing can provide an avenue for controlling the electronic, electrical, optical, and thermal properties.

The performance characteristics of $MoS_2$ sheets could be improved by incorporation of semiconductor nanoparticles with good distribution. $MoS_2$ sheets decorated with nanoparticles might result in particular properties due to synergetic effects [19, 20]. $MoS_2$ nanosheets decorated with semiconductor nanoparticles have recently been reported [19-21]. Heterostructured catalysts exhibit better performance and have proved more effective compared to individual catalysts [13, 22]. One of the most difficult challenges in the development of heterostructured photocatalysts is finding specific materials that have both high photocatalytic activity and suppressed recombination effects for pollutant degradation.

$MoS_2$ nanosheets with well-distributed semiconductor nanoparticles can offer more versatility for charge-carrier transportation and selective catalysis. This effects result from the greater specific surface area and porosity. Thus, $SnO_2$-decorated $MoS_2$ composites may provide new opportunities to develop new photocatalyst materials.

To the best of our knowledge, there have been no reports about the synthesis of $SnO_2$ incorporated on $MoS_2$ nanosheets as a photocatalyst. We report a two-step method for synthesizing such nanosheets and used them as a photocatalyst for the first time. The metal-interfacing mechanism and its influence on the structural and photocalaytic properties of $SnO_2$@$MoS_2$ are discussed. The greatest advantage of this method is that mesoporous $SnO_2$ nanoparticles are formed via wet oxidation-reduction reaction between metal precursors in

the presence of CTAB. Photocatalysis experiments prove that this heterogeneously structured composite has higher photocatalytic activity than pristine $MoS_2$.

**Experimental Procedure**

All chemicals were analytical grade and used as received without further purification.

**Preparation of $MoS_2$ nanosheets**

To obtain the $MoS_2$ nanosheets, ammonium hepta molybdate tetrahydrate, citric acid, and thiophene ($C_4H_4S$) were used as the starting materials and sulfur source. 2.05 g of ammonium heptamolybdate tetra hydrate and 1.56 g of citric acid were dissolved in distilled water and magnetically stirred for 10 min at 90˚C on a hot plate to form a homogeneous solution. The white suspension was vigorously stirred and the pH was adjusted to 3.5 with the addition of ammonia water. Then, 3.15 g of thiophene in water was added dropwise to the solution and transferred to an autoclave, which was maintained at 200˚C for 10 h. After natural cooling of the reactor down to 25˚C, the resulting precipitates were collected through centrifugation, filtered, and washed three times with distilled water and acetone. The final precipitates were dried under vacuum at 130˚C for 2 h.

**Preparation of $MoS_2$ sheets decorated with $SnO_2$ nanoparticles**

The $MoS_2$ precipitates (20 mg) were exfoliated in distilled water (25 mL) and heated at 75˚C under magnetic stirring for 30 min to form a colloidal suspension. Then, $SnCl_2{\bullet}2H_2O$ (2.7 g) was dissolved in the colloidal solution. HCl (1.3 mL) and $H_2O$ (30 mL) were added drop-wise to the solution with continuous heating and stirring for 2 h. After several trials, we optimized the concentration of CTAB to 0.05 mmol. 0.05 mmol of CTAB was added to the suspension and stirred at 110˚C for 6 h. The final products were collected, filtered, and washed three times with acetone. The obtained precipitates were dried in a vacuum oven at 120˚C for 12 h.

**Characterization of samples**

The structural properties of the obtained precipitates were characterized by powder X-ray diffraction (XRD) with a Shimadzu Labx XRD 6100 using Cu-Kα radiation (λ=0.14 nm). The scan range was 10–80˚, and the scan speed was 5 deg/min. The nanoparticles were

analyzed with a transmission electron microscope (TEM, Hitachi H-7000) at 110 kV and a high-resolution TEM (HRTEM, Tecnai $G^2$ F 20 S-Twin TEM) at an accelerating voltage of 210 kV. The optical properties of the nanoparticles were studied using UV-visible spectroscopy (Cary 5000 UV-Vis spectrophotometry). Thermogravimetric (TG) and differential thermal analysis (DTA) were carried out on a SDT Q600 thermogravimetric analyzer under $N_2$ flow at a rate of 28 $cm^3$/min. The furnace temperature was increased from room temperature to 900˚C at a heating rate of 6˚C per minute. The specific BET surface area and pore size distribution were determined by $N_2$-adsorption using the BJH method with a Micrometrics ASAP 2000 instrument. The purity of the final product was examined by an Avatar 370 Fourier transform infrared spectroscope (FTIR) with a spectral range of 4000–400 $cm^{-1}$ and X-ray photoelectron spectroscopy (XPS, Thermo Scientific K-alpha surface analysis instrument). Electrochemcial impedance spectroscopy (EIS) measurements were carried out on a CHI 630B workstation. The measurement was conducted in 0.1 M KCl solutions containing 3 mM $K_3$ [Fe (CN) $_6$]/$K_4$ [Fe (CN) $_6$].

Photocatalytic experiments were performed at the natural pH of a solution of Rhodamine B (RhB), an organic pollutant. The experiments involved a photoreactor that has a 150-W mercury lamp with a main emission wavelength of 254 nm as an internal light source, which is surrounded by a quartz vessel. The light source is completely surrounded by a suspension of the $SnO_2$-decorated $MoS_2$ nanosheet catalyst and aqueous RhB (100 mL, 10 mg/L). Before irradiation, the suspension was stirred in the dark for 15 min to obtain a good dispersion and to ensure adsorption-desorption equilibrium between the organic pollutant molecules and the catalyst. During light irradiation, the samples of the reaction solution were collected at particular intervals and examined using an optical spectrophotometer.

**Results and discussion**

Fig. 1 shows the formation mechanism of the $SnO_2$-decorated $MoS_2$ nanocomposite and processing conditions. CTAB cationic surfactant was used to obtain the mesoporous $SnO_2$ nanoparticles. The optimized concentration of CTAB is 0.3 mmol, and the effect of CTAB in the formation of the mesoporous structured $SnO_2$ particles was elucidated. After addition of a small account of CTAB, aggregation of $CTA^+$ ions occurs on the surface of $MoS_2$ nanosheets. A few $CTA^+$ ions form a complex structure on the surface, and excess CTA+ ions go to the air-water interface to generate mesoporous structured $SnO_2$ particles [23, 24]. This result

suggests that the $CTA^+$ ions interact with the $MoS_2$ units of the molecules and are involved in the assembly process to create the mesostructures. Also, CTAB plays an important role in the assembly process of $SnO_2$ and $MoS_2$ nanosheets.

The powder XRD patterns of the pristine $MoS_2$ and $SnO_2$-decorated $MoS_2$ nanosheets are shown in Fig. 2. The diffraction peaks of pristine $MoS_2$ (2θ =14.1˚, 28.4˚, 32.9˚, 39.5˚, 49.4˚, 55.4˚, 58.6˚, and 69.4˚) matched with the JCPDS card (No. 75-1539) and were confirmed by previous reports [25, 26]. In the case of $SnO_2$-decorated $MoS_2$, the main diffraction peaks coincided well with those of pristine $MoS_2$, and $SnO_2$ peaks also appeared with high intensity. This is attributed to the high dispersion of $SnO_2$ on the surface of $MoS_2$. The average crystallite size of $MoS_2$ and $SnO_2$-decorated $MoS_2$ was determined based on the (102) peak using the Debye-Scherrer formula [27]. The crystallite sizes were 23.53 nm and 27.46 nm for pristine $MoS_2$ and $SnO_2$-decorated $MoS_2$, respectively. The crystallite size of $MoS_2$ slightly increased after surface modification with $SnO_2$.

FESEM images of pristine $MoS_2$ and $SnO_2$-decorated $MoS_2$ are shown in Fig. S1 (a-d). The shape of pristine $MoS_2$ is a sheet form and it is completely agglomerated. The $SnO_2$-decorated $MoS_2$ is composed of both spherical ($SnO_2$) and sheet ($MoS_2$) shapes. $SnO_2$ appeared as bright spheres with mesoporous structure, while the $MoS_2$ appeared as gray sheets. Tiny $SnO_2$ spheres were deposited on the $MoS_2$ sheet surface, which was confirmed by the XRD results. TEM and HR-TEM images of pristine $MoS_2$ and $SnO_2$-decorated $MoS_2$ are shown in Fig. 3. The TEM images confirm that the $SnO_2$ particles are aggregated on the $MoS_2$ sheets. For $MoS_2$ nanosheets of a length more than 300 nm, their thickness is around 20–100 nm. It is clear that the $SnO_2$ particles are spread on the $MoS_2$ sheets, which is in good agreement with the FESEM results. The lattice fringes of the $SnO_2$-decorated $MoS_2$ have lattice spacing of 0.61 and 0.33 nm, which can be ascribed to the (002) and (110) planes of 2H-$MoS_2$ and $SnO_2$, respectively. The elements present were detected using EDX analysis, as shown in Fig. S2. Mo, Sn, S, and O elemental peaks can clearly be seen for the $SnO_2$-decorated $MoS_2$ sample. This result also confirms that $SnO_2$ spheres are randomly deposited on the $MoS_2$ surface. No other elements appeared, and the present elements were observed at their consistent KeV values. The atomic percentage of all the elements was further confirmed by XPS analysis. HRTEM mapping analysis was done to further understand the distribution and elements present in the $SnO_2$-decorated $MoS_2$ nanocomposite, as shown in Fig. S2 (c-g). Mo, Sn, S, and O are predominately distributed within the selected area of the $SnO_2$-

decorated $MoS_2$ sample, which is in good agreement with the FESEM-EDX results.

TG analysis and DTA of the $SnO_2$-decorated $MoS_2$ nanocomposite were performed in nitrogen atmosphere, as shown in Fig. S3. The weight loss of 2.1% between room temperature and 150˚C is ascribed to residual solvent evaporation, which favors crystal growth. The weight loss of 9.1% between 150˚C and 390˚C is due to the dehydroxilation process of the sample. Dehydroxilation promotes the partial breaking of sulfur and hydrogen when in contact [28]. These phenomena give rise to the small exothermic peak centered at 355˚C in the DTA curve. Sulfur breaking during dehydroxylation favored the formation of strong Mo-O-Sn bonds. The small exothermal peaks between 390˚C and 780˚C in the DTA curve are attributed to the recrystallization and deformed nanocrystals. Negligible endothermic peaks appeared above 590˚C. Further sintering above 630˚C caused more transformations that generated more weight loss and one more exothermic peak. The total weight loss at 900˚C for the $SnO_2$-decorated $MoS_2$ sample is 21%, indicating that it was stable with temperature.

The FT-IR spectra of the $SnO_2$-decorated $MoS_2$ nanocomposite are shown in Fig. S4. The bands at 3404, 3143, 1647, 1410, and 603 $cm^{-1}$ are associated with pristine $MoS_2$ nanomaterials [21, 29]. Among these, an absorption band at 3154 $cm^{-1}$ was generated by the stretching vibration of hydroxyls [30]. However, when the sample is heated at 400˚C, this peak disappeared, which is in good agreement with the TG-DTA results. The band at 1410 $cm^{-1}$ corresponds to in-plane bending vibration of O-H [31]. The absorption bands at about 1647 and 603 $cm^{-1}$ are ascribed to the in-plane $OH^-$ group bending vibration and $\gamma_{as}$ Mo-S vibration, respectively [32]. New peaks were obtained from the $SnO_2$-decorated $MoS_2$ nanocomposite. The band at 938 $cm^{-1}$ is assigned to $\gamma_{as}$ Mo-O vibration, the one at 720 $cm^{-1}$ is attributed to out-of-plane bending vibration of $OH^-$ [29], and the one at 603 $cm^{-1}$ is attributed to stretching vibration of Sn-O [33].

The specific area and pore volume of the $SnO_2$-decorated $MoS_2$ nanosheets were measured using nitrogen adsorption. The $N_2$ adsorption-desorption isotherm in Fig. 4 shows that the surface area and pore volume (inset) of $SnO_2$-decorated $MoS_2$ nanosheets were 103.7 $m^2/g$ and 0.16 $cm^3/g$ respectively. This indicates moderate $N_2$ adsorption capability due to the $SnO_2$ nanoparticles being mesoporous. A hysteresis loop appears when the relative pressure is higher than 0.87 and is ascribed to capillary condensation in the mesopores. This is also in

good agreement with the FESEM results.

The X-ray photoelectron survey spectra of pristine $MoS_2$ and the $SnO_2$-decorated $MoS_2$ nanocomposite are shown in Fig. S5. Mo 3d, Mo 3p, and S2p peaks were obtained from pristine $MoS_2$, whereas additional peaks of Sn 3d, Sn 3p, and O1s appeared for the $SnO_2$-decorated $MoS_2$ nanocomposite. The XPS analysis confirms that the as-obtained $SnO_2$-decorated $MoS_2$ nanocomposite is composed of pristine $MoS_2$ and $SnO_2$. Fig. S6 shows the high-resolution spectra of individual elements of the as-obtained $SnO_2$-decorated $MoS_2$ nanocomposite. The main comparison between pristine $MoS_2$ (Mo $3d_{5/2}$ = 228.45 eV, Mo $3d_{3/2}$ =231.17 eV, S $2p_{3/2}$ = 161.31 eV) [34] and $SnO_2$-decorated $MoS_2$ (Mo $3d_{5/2}$ = 228.86 eV, Mo $3d_{3/2}$ = 231.83 eV, S 2p3/2 =161.69 eV, Sn$3d_{5/2}$ =487.38 eV) [35] reveals that both the Mo $3d_{5/2}$ and S $2p_{3/2}$ peaks shifted significantly to higher binding energies (BE) by about 0.41 eV and 0.38 eV, respectively, which is ascribed to the formation of the hybrid structure.

The difference in BE (ΔBEsn-s) obtained for the $SnO_2$-decorated $MoS_2$ nanocomposite was 325.69 eV, which varied according to the tin content and preparation conditions [35]. The main concentrations of S for both pristine $MoS_2$ and the $SnO_2$-decorated $MoS_2$ nanocomposite are about 38.1 with negligible reduction. In addition, the O 1s peak (531.1 eV) of the $SnO_2$-decorated $MoS_2$ sample shifted to higher binding energy by about 0.24 eV (O 1s = 531.34 eV) due to formation of the heterogeneous compound. The higher energy peak is associated with $O_3^-$ and the formed Sn-Mo-S phase of the sample. The existence of apical $S^{2-}$ and terminal $S^{2-}$ suggests that an S-rich $MoS_2$ structure in the $SnO_2$-decorated $MoS_2$ nanocomposite. It was reported that $MoS_2$ with more active S edge sites is highly active for catalytic applications [6, 36]. The mesoporous $SnO_2$ has increased active sites for enhancing the photocatalytic activity.

The UV-vis absorption edge of the semiconductor catalyst depends on the electronic structure feature. The optical absorption properties of pristine $MoS_2$ and $SnO_2$-decorated $MoS_2$ nanocomposite were analyzed, and the diffuse absorption spectrum is shown in Fig. S7. The pristine $MoS_2$ had a weak UV response with an absorption band edge at 220 nm. In the case of the $SnO_2$-decorated $MoS_2$ nanocomposite, the light absorption is enhanced with a slight red-shift in the absorbance region, which is ascribed to the high absorption ability of $SnO_2$ in UV light. This red-shift is caused by the presence of $SnO_2$ mesoporous nanoparticles in the composite, resulting in a possible charge-transfer transition between $SnO_2$ and $MoS_2$

[37]. The intensity of optical absorption was enhanced, and the optical absorption edges of the $SnO_2$-decorated $MoS_2$ nanocomposite were extended. This result favors the photocatalytic activity of the $SnO_2$-decorated $MoS_2$ nanocomposite.

The band gap energy of pristine $MoS_2$ and $SnO_2$-decorated $MoS_2$ nanocomposite can be estimated from a plot of $(\alpha h\upsilon)^{1/2}$ versus the photon energy. The intercept of a tangent to the x-axis was recorded, which gives the band gap energies of the sample, as shown in Fig. 5. The estimated band gap energies of pristine $MoS_2$ and the $SnO_2$-decorated $MoS_2$ nanocomposite were approximately 2.31 eV and 2.21 eV, respectively.

The variation in the absorption spectrum of RhB (10 ppm) with respect to irradiation time using 50 mg/L of $SnO_2$-decorated $MoS_2$ is shown in Fig. 6. The absorption maximum obtained at 556 nm decreases gradually when the irradiation time increases. The adsorption peak nearly disappeared and the red color of the RhB pollutant faded after 50 min of irradiation, which indicates the complete degradation of RhB. The results obtained with pure $SnO_2$, $MoS_2$, and $SnO_2$-decorated $MoS_2$ in the photocatalytic degradation of RhB under UV light irradiation are shown in Fig. 7. The blank experiment was carried out without any photocatalyst and result showed that hardly degraded and its degradation percentage is below 4.3% after 50 min of exposure (Fig.7). In contrast, when the photocatalyst is added and noticeable RhB degradation occurred. No significant concentration decay occurred when keeping the $SnO_2$-decorated $MoS_2$ suspension in dark conditions for 50 min. it can be seen from Fig.7, the pure $SnO_2$ showed lower photocatalytic activity compared to pristine $MoS_2$. The order of degradation rates of RhB pollutant is $SnO_2$-decorated $MoS_2$ > pristine $MoS_2$> pure $SnO_2$. It is clear that the coupled $SnO_2$-$MoS_2$ photocatalyst demonstrated higher photocatalytic activity than pure $SnO_2$ and $MoS_2$. Hence, the $SnO_2$ content should be a significant factor affecting the photocatalytic reaction of the $SnO_2$-decorated $MoS_2$ nanosheets. The degradation of RhB pollutant occurs as a photocatalytic process, and the $SnO_2$-decorated $MoS_2$ is more efficient than the pure forms of $SnO_2$ and $MoS_2$, as shown by the degradation curve in Fig. 7.

The kinetic fitting semilog plot of -ln ($C/C_0$) with respect to irradiation time is shown in Fig. 8. If the concentration of pollutant is proportional to the reaction rate or the pollutant concentration is in the millimolar range, the effective reaction rate constant (k) of the photocatalytic reaction is calculated by assuming a pseudo-first-order kinetic law: $C/C_0 = \exp$

(-kt) [6, 38]. The value of k was determined to be 0.0072 and 0.047 $min^{-1}$ for the $MoS_2$ and $SnO_2$-decorated $MoS_2$ catalyst, respectively. The $SnO_2$-decorated $MoS_2$ nanocomposite showed significantly more activity in photocatalyzing the degradation of RhB than the pure $SnO_2$ and $MoS_2$ nanoparticles, which is ascribed to the specific surface area of the $SnO_2$-decorated $MoS_2$ nanocomposite. In addition, the mesoporous structure of $SnO_2$ nanoparticles may also contribute to suppressing the recombination effect.

The XRD peaks of the $MoS_2$ nanoparticles show somewhat larger widths than that of the $SnO_2$-decorated $MoS_2$ nanocomposite. This indicates that $MoS_2$ has a higher degree of crystallite agglomeration along with a larger number of grain boundaries, which may accelerate the electron-hole recombination. Therefore, the photodegradation of pollutant is much faster with the $SnO_2$-decorated $MoS_2$ nanocomposite rather than the $MoS_2$ catalyst. In addition, the $SnO_2$-decorated $MoS_2$ heterogeneous structure could facilitate the rectification of photogenerated charge carriers, as was demonstrated in previous studies. Examples are $MoS_2$ and $WS_2$ supported by $SiO_2$ and $TiO_2$ [39], $MoS_2$ developed on $TiO_2$ [40], and $MoS_2$ on CdS [41].

The stability and reusability of a sulfide photocatalyst are significant matters of concern. Sulfide photocatalysts exhibit activity loss due to corrosion during the photooxidation reactions. Hence, it is important to verify the reusability of the photocatalyst. To check this, a fixed portion of $SnO_2$-decorated $MoS_2$ nanocomposite was recycled four times in the photocatalytic RhB degradation reaction under UV light irradiation while restoring the RhB concentration after 50 min by the addition of pristine compound to the solution. The RhB concentration was measured before and after completion of each cycle. The results are shown in Fig. 9, which clearly shows that even after the fourth cycle, the photocatalyst continues to be highly active.

The RhB concentration remaining after the first run (0.3%) is compared with the value for the fourth run (1.6%) in Fig. 9. After the last of these cycles, the nanocomposite was tested again for photocatalytic activity, and the apparent constant was $k = 0.036\ min^{-1}$, which is lower by 11% than that measured for the fresh sample. When the same experiment was performed using pristine $MoS_2$ nanoparticles, the loss of activity was very high, and more importantly, the concentration of RhB remaining in the solution increased from 61% in the first run to 78% in the fourth one.

In order to observe the relevant changes in composition and redox state of $SnO_2$-decorated $MoS_2$ nanocomposite after the four cyclic photodegradation, an XPS analysis was carried out and results are presented in Fig.10. The used nanocomposite shows a small broad peak compared to fresh sample at $E_B$= 234.25 eV. $E_B$ values above 234.25 eV are rarely reported in Mo compound, which is attributed to Mo bound to a ligand with lower electron donating capability [35, 36, 42]. The S2p region a small compound peak appears at $E_B$ = 163.4 eV in the $2p_{3/2}$ peak, which is ascribed to oxidation of sulphide species. This indicate that possible reaction and formation of a bond with RhB and to enhance the degradation of pollutant. However, the consequence of these changes on the photoreaction is moderate. As a result, $SnO_2$-decorated $MoS_2$ nanocomposite has higher stability even after cyclic photoreaction due to their cohesive energies with strong Madelung lattice energies [36, 42] and structural features, thanks to the higher charge and possible numbers of M-S bonds on the Sn cations. The XPS results of $SnO_2$-decorated $MoS_2$ nanocomposite before and after photoreaction do not show the presence of pollutant in it, which reflect the complete mineralization of the pollutant.

In order to provide further evidence for proposed mechanism, EIS studies were conducted. It was observed from Fig. 11, the arc radius in the impendence spectrum of the $SnO_2$-decorated $MoS_2$ nanocomposite is smaller than the arc radius of the pristine $MoS_2$ sample in the spectrum, which indicates that the $SnO_2$-decorated $MoS_2$ nanocomposite has a lower resistance than pristine $MoS_2$, similar results have been reported [43, 44]. This can attributed to the $SnO_2$@$MoS_2$ heterostructured interface can facilitate the interfacial electron-hole pairs transfer process [43-46].

**Photocatalytic mechanism**

The schematic mechanism of photogenerated electron-hole transfer process in $SnO_2$-decorated $MoS_2$ nanosheets under UV- light irradiation was proposed and it shown in Fig. 12. For $MoS_2$ with the band gap energy of 2.31 eV, but it shows little photocatalytic activity due to the fast recombination effect of the electron/hole pairs in $MoS_2$ under UV irradiation in the current experimental conditions. The conduction band (CB) of $MoS_2$ is lower than that of $SnO_2$; hence the former can turn as a sink for the photogenerated electrons [43-47]. Then, the photogenerated holes might be trapped within the $SnO_2$ particles due to the holes move in the opposite direction from the electrons. As a result, the recombination of the electron/hole pairs

is suppressed and, consequently the $SnO_2$-decorated $MoS_2$ nanocomposite exhibits higher photocatalytic activity than that of pure $SnO_2$ and $MoS_2$.

The enhancement in photocatalytic activity of the $SnO_2$-decorated $MoS_2$ nanocomposite can be explained based on two mechanisms. The first is the adsorption ability of the $MoS_2$ nanosheets, since the adsorption is a key process in the catalytic destruction of pollutant. Second is the electron transfer from $SnO_2$ to the $MoS_2$ nanosheets. It is well know that a metal oxide semiconductor with greater photon energy could promote an electron from the valence band (VB) to the conduction band (CB) [46-49]. The promoted electron creates a vacancy in the VB and a positive hole and resulting, the separation of the photogenerated electrons and holes was accomplished at the composite interface. This positive hole can react with hydroxyl groups and form a hydroxyl radical (•OH), a powerful oxidant. The promoted electrons decrease the dissolved oxygen and yield superoxide anion radicals ($O_2^{\bullet-}$) [47].

The $SnO_2$-decorated $MoS_2$ heterogeneous structure facilitates the effective electron transfer from the CB into the $MoS_2$ nanosheets and suppresses the recombination effect. This proposed mechanism is supported by the higher photocatalytic activity of the $SnO_2$-decorated $MoS_2$ nanocomposite. The major proposed reaction steps during the photocatalytic process are as follows:

$SnO_2 + h\upsilon \rightarrow SnO_2 (e^- + h^+)$

$SnO_2 (e^-) + MoS_2 \rightarrow SnO_2 + MoS_2 (e^-)$

$MoS_2 (e^-) + O_2 \rightarrow + MoS_2 + \bullet O_2^-$

$SnO_2 (h^+) + OH^- \rightarrow SnO_2 + \bullet OH$

$O_2 + e^- \rightarrow \bullet O_2^- \rightarrow \bullet OH$

$RhB + \bullet O_2^-/\bullet OH \rightarrow$ Products

$RhB + h^+ \rightarrow CO_2 + H_2O +$ by products

Another reason for the lower photocatalytic activity of the individual $MoS_2$ nanoparticles is that they react with dissolved organic matter and with the surface sulfide ions. This gives rise to sulfate ions and dissolution of the solid. This phenomenon occurs due to photocorrosion and results in lower photocatalytic performance.

## Conclusions

We have reported a solvothermal method for effective decoration of $MoS_2$ nanosheets with $SnO_2$ mesoporous nanoparticles. The characterization results reveal that the $SnO_2$ mesoporous nanoparticles are distributed on the $MoS_2$ nanosheet surface and form $SnO_2$@$MoS_2$ hetero nanostructures. The $SnO_2$-decorated $MoS_2$ nanocomposites are formed by Van der Waals interaction. The morphology and density of the semiconductor nanoparticles can be tuned by changing the defective sites in $MoS_2$ nanosheets. The result of the photocatalyst test shows that the nanocomposite has outstanding photocatalytic activity with excellent stability compared to pristine $MoS_2$ and $SnO_2$ catalyst. The architecture of the nanocomposite makes a prominent contribution to the excellent photocatalytic performance.

## Acknowledgements

This research was supported by the Basic Science Research Program through the National Research Foundation of Korea (NRF) and funded by the Ministry of Science ICT and Future Planning (2014R1A2A2A01007081).

## Notes and References

[1] R. Tenne, L. Margulis, M. Genut, and G. Hodes, Nature, 1992, **360**, 444-446.

[2] C.N.R. Rao, and M. Nath, Dalton Trans., 2003, **1**, 1-24.

[3] Th. F. Jaramillo, K. P. Jørgensen, J. Bonde, J. H. Nielsen,S. Horch, and Ib. Chorkendorff , Science, 2007, **317**, 100-102.

[4] S. V. P. Vattikuti, Ch. Byon, Ch. V. Reddy, B. Venkatesh, and J. Shim, J. Mater. Sci., 2015 **50**, 5024–5038

[5] N. A. Dhas, A. Ekhtiarzadeh, and K. S. Suslick, J. Am. Chem. Soc., 2001, **123**, 8310-8316.

[6] S.V. P. Vattikuti, Ch. Byon, and Ch. V. Reddy, Superlattice. Microst., 2015, **85**, 124–132.

[7] M. A. Albiter, R. Huirache-Acuña, F. Paraguay-Delgado, J. L. Rico and G. Alonso-Nuñez, Nanotechnol., 2006, **17**, 3473–3481.

[8] S. V. P. Vattikuti, Ch. Byon, Ch. V. Reddy, J. Shim, and B. Venkatesh, Appl. Phys. A, 2015, **119**, 813–823.

[9] D. Voiry, M. Salehi, R. Silva, T. Fujita, M. Chen, T. Asefa, V. B. Shenoy, G. Eda, and M. Chhowalla, Nano Lett., 2013, **13**, 6222−6227.

[10] X. Wang, Zh. Zhang, Y. Chen, Y. Qu, Y. Lai, and J. Li, J. Alloy. Compd., 2014, **600**, 84–90.

[11] Z. Zeng, Z. Yin, X. Huang et al., Angewandte Chemie., 2011, **50**, 11093–11097.

[12] M-L. Tsai, Sh-H. Su, J-K. Chang, D-Sh. Tsai, Ch-H. Chen, Ch-I. Wu,L-J.Li, L-J. Chen, and Jr-H. He, ACS nano, 2014, **8**, 8317-8322.

[13] Q.V. Le, Th. Ph. Nguyen, H. W. Jang and S. Y. Kim, Phys. Chem. Chem. Phys., 2014,**16**, 13123-13128.

[14] H. S. Lee, S.-W. Min, Y.-G. Chang et al., Nano Lett., 2012, **12**, 3695–3700.

[15] H. Li , J. Wu , Z. Yin , and H. Zhang, Acc. Chem. Res., 2014, **47 (4)**, 1067–1075.

[16] J. N. Coleman, M. Lotya, A. Orçöneill, S. D. Bergin, P.J. King, U. Khan, K. Young, A. Gaucher, S. De, R. J. Smith, I. V. Shvets, S. K. Arora, G. Stanton, H. Y. Kim, K. Lee, G. T. Kim,; G.S. Duesberg, T. Hallam, J. J. Boland, J. J. Wang, J. F. Donegan, J. C. Grunlan, G. Moriarty, A. Shmeliov, R. J. Nicholls, J. M. Perkins,; E.M. Grieveson, K. Theuwissen, D. W. McComb, P. D. Nellist, and V.Nicolosi, Science, 2011, **331 (6017)**, 568−571.

[17] Y. Huang, Y.-E Miao, L. Zhang, W. W. Tjiu, J. Pan, and T. Liu, Nanoscale, 2014, **6**, 10673.

[18] X. Yang, W. Liu, M. Xiong, Y. Zhang, T. Liang, J. Yang, M. Xu, J. Ye and H. Chen, J. Mater. Chem. A, 2014, **2**, 14798-14806

[19] Xiaojia Liu, Liping Li, Yuanjie Wei, Yizhi Zheng, Qian Xiao and Bo Feng, Analyst, 2015, **140**, 4654-4661

[20] Z. Chen, D. Cummins, B. N. Reinecke, E. Clark, M. K. Sunkara and T. F. Jaramillo, Nano Lett., 2011, **11**, 4168–4175.

[21] X. Wu, X.Yan, Y. Dai, J.Wang, J. Wang, and X. Cheng, Mater. Lett., 2015, **152**, 128–130.

[22] H. Li, K. Yu, X. Lei, B. Guo, Ch. Li, H. Fu and Z. Zhu, Dalton Trans., 2015, **44**, 10438

[23] A. S. Poyraz, C. Albayrak, and Ö. Dag, T, Micropor. Mesopor. Mater., 2008, **115**, 548–555,

[24] A. S. Poyraz and O¨.Dag, J. Phys. Chem. C, 2009, **113**, 18596–18607.

[25] M. Wu, Y. Wang, X. Lin, N. Yu, L. Wang, L. Wang, A. Hagfeldt and T. Ma, Phys. Chem. Chem. Phys., 2011, **13**, 19298–19301.

[26] D. Duphil, S. Bastide, and C.L. Clement, J. Mater. Chem., 2002, **12**, 2430–2432.

[27] L.Alexander and H. P. Klug, J. Appl. Phys., 1950, **21**, 137-142.

[28] X. Bokhimi, J.A. Toledo, J. Navarrete, X.C. Sun, and M. Portilla, Int. J. Hydrogen. Energ. 2001, **26**, 1271–1277.

[29] L. Zhou, B. He, Y. Yang, and Y. He, RSC Adv., 2014, **4**, 32570-32578

[30] N. Ahmad, S. Maitra, B.K. Dutta, F. Ahmad, J. Environ. Sci., 2009, **21**, 1735–1740.

[31] H. Wang, P. Chen, F. Wen, Y. Zhu, and Y. Zhang, Sensor. Actuat. B, 2015, **220**, 749–754

[32] E. Menart, V. Jovanovski, and S.B. Ho˘cevar, Electrochem. Commun., 2015, **52**, 45–48.

[33] K. Karthikeyana, S. Amaresha, D. Kalpanab, R. Kalai Selvanc, and Y.S. Lee, J.Phys.Chem.Solids., 2012, **73**, 363-367.

[34] P. Ilanchezhiyan, G. Mohan Kumar, and T.W. Kang, J. Alloy. Compd., 2015, **634 (2)** 104–108.

[35] J. Iranmabbob, D.O. Hill, and H. Toghiani, Appl. Surf. Sci., 2001, **185**, 72-78.

[36] L.P. Zhu, H.M. Xiao, X.M. Liu, S.Y. Fu, J. Mater. Chem., 2006, **16**, 1794–1797.

[37] Q.Q. Wang, B. Z. Lin, B.H. Xu, X.L. Li, Z. J. Chen, and X.-T. Pian, Micropor. Mesopor. Mater., 2010, **130**, 344–351

[38] R. Lucen, F. Fresno, and J. C. Cones, Appl. Catalys. A: General, 2012, **415– 416**,111–117

[39] D. James, and T. Zubkov, J. Photoch Photobio. C., 2013, **262**, 45– 51.

[40] W. Ho, J.C. Yu, J. Lin, J. Yu, and P. Li, Langmuir, 2004, **20**, 5865–5869.

[41] X. Zong, X. Yan, G. Wu, G. Ma, F. Wen, L. Wang, and C. Li, J.Am. Chem. Soc. 2008, **130**, 7176–7177.

[42] R. Lucena, F. Fresno, J.C. Conesa, Appl. Catalys. A: General, 2012, **415– 416**, 111– 117.

[43] W. Cui, W. An, L. Liu, J. Hu, and Y. Liang, J. Hazard. Mater., 2014, **280**, 417-427.

[44] J. Di, J. Xia, Y. Ge, L. Xu, H. Xu, J. Chen, M. He and H. Li, Dalton Trans., 2014, **43**, 15429-15438.

[45] Y. Zhuo, J. Huang, L. Cao, H. Ouyang and J. Wu, Mater. Lett., 2013, **90**, 107–110.

[46] Y. Chen, X. Cao, J. Kuang, Zh. Chen, J. Chen, and B. Lin, Catalys. Commun., 2010, **12**, 247-250.

[47] Y. Liang, Sh. Lin, L. Liu, J. Hu, and W. Cui, Appl. Catalys. B: Environ., 2015, **164**, 192-203.

[48] V. Gupta and T. A. Saleh, Dr. Stefano Bianco (Ed.), 2011, ISBN: 978-953-307-500-6, InTech.

[49] J. Li, K. Yu, Y. Tan, H. Fu, Q. Zhang, W. Cong, Ch. Song, H. Yin and Z. Zhu, Dalton Trans., 2014, **43**, 13136-13144.

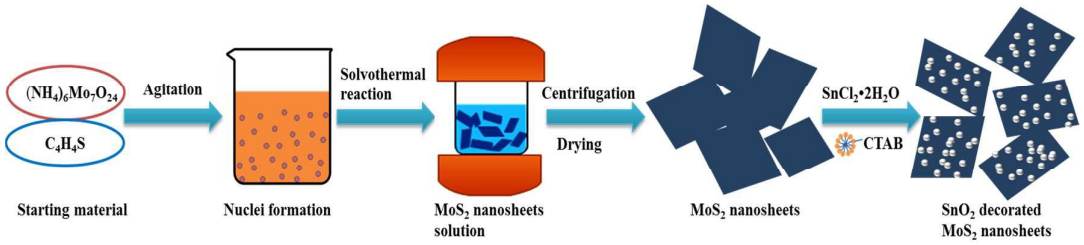


Fig.1 Schematic illustration of the synthesis method of $SnO_2$ decorated $MoS_2$ nanosheets

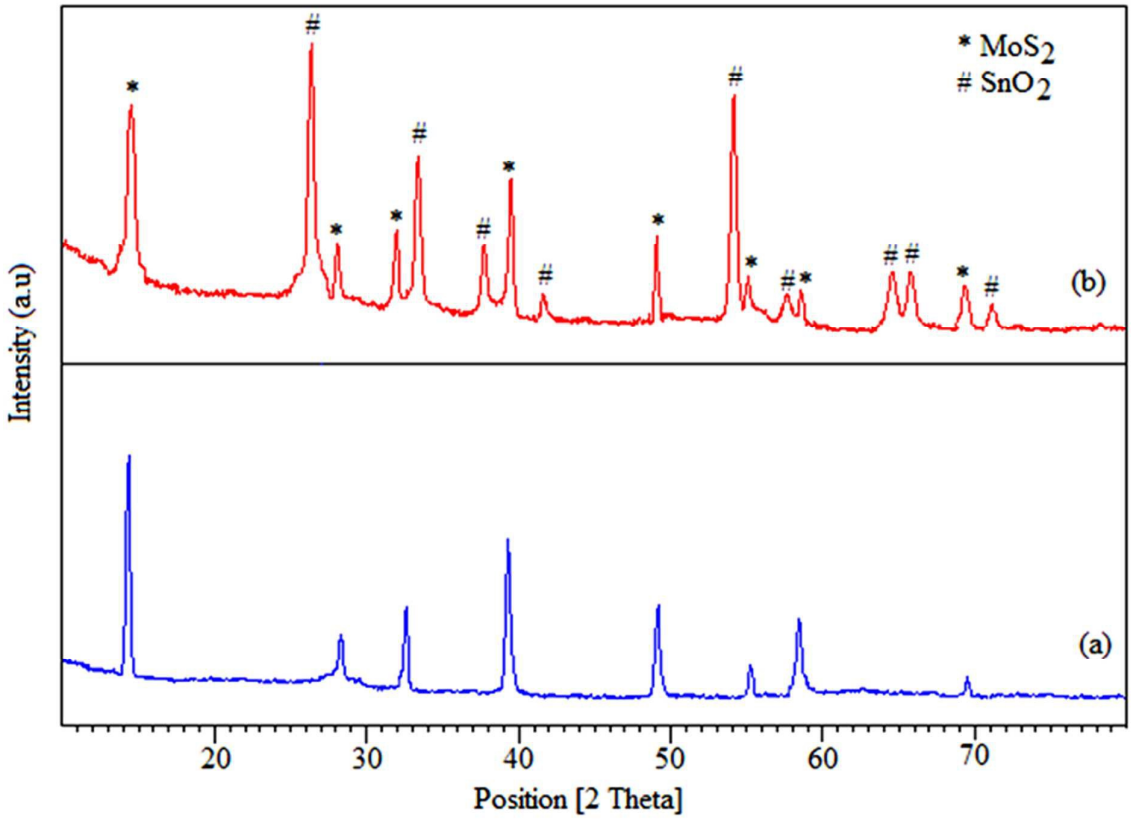


Fig.2. XRD patterns of: (a) pristine $MoS_2$ and (b) $SnO_2$-decorated $MoS_2$ nanocomposite

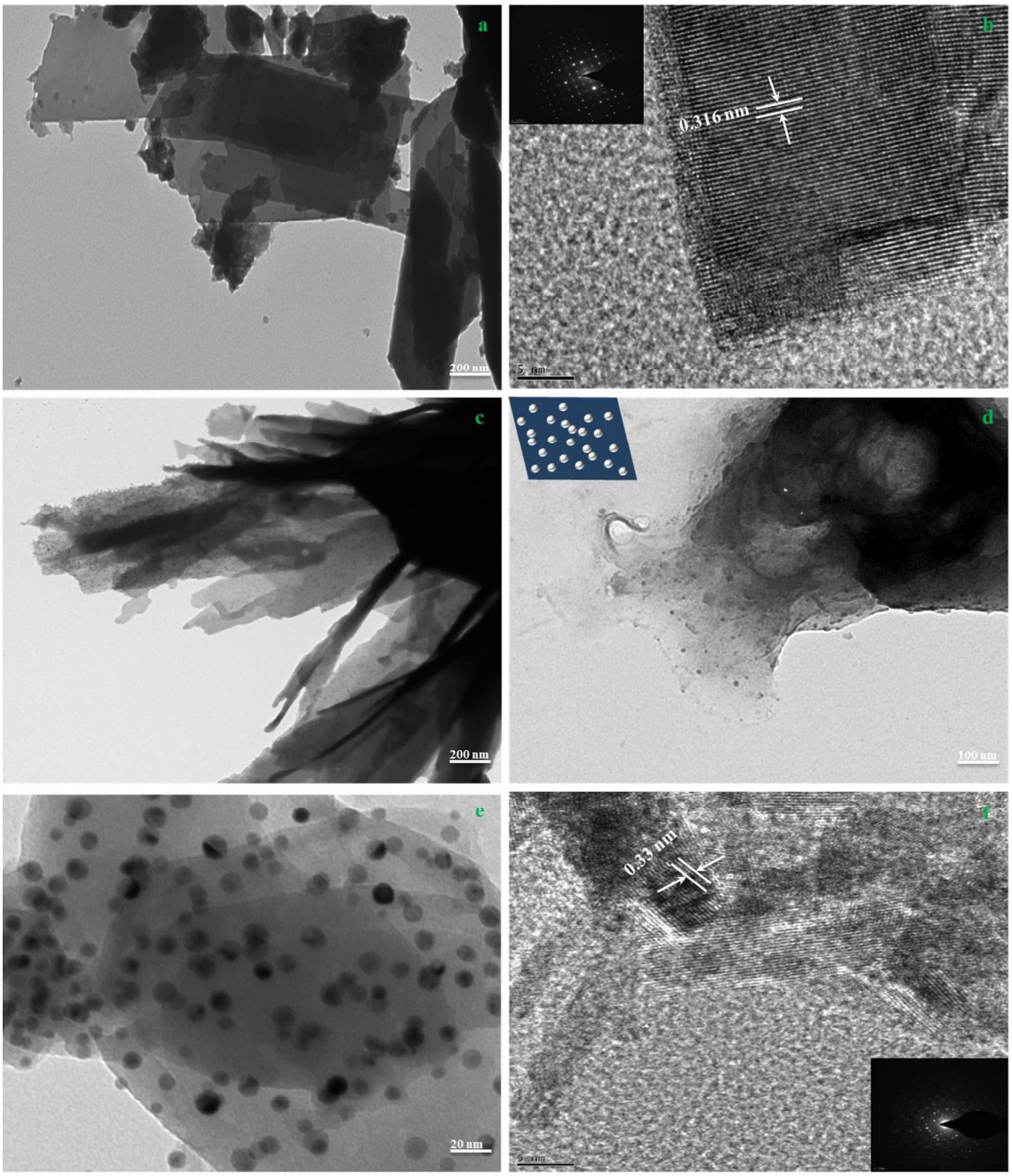


Fig.3. TEM and HRTEM images of (a), (b) pristine $MoS_2$, (c) - (f) $SnO_2$-decorated $MoS_2$ nanocomposite

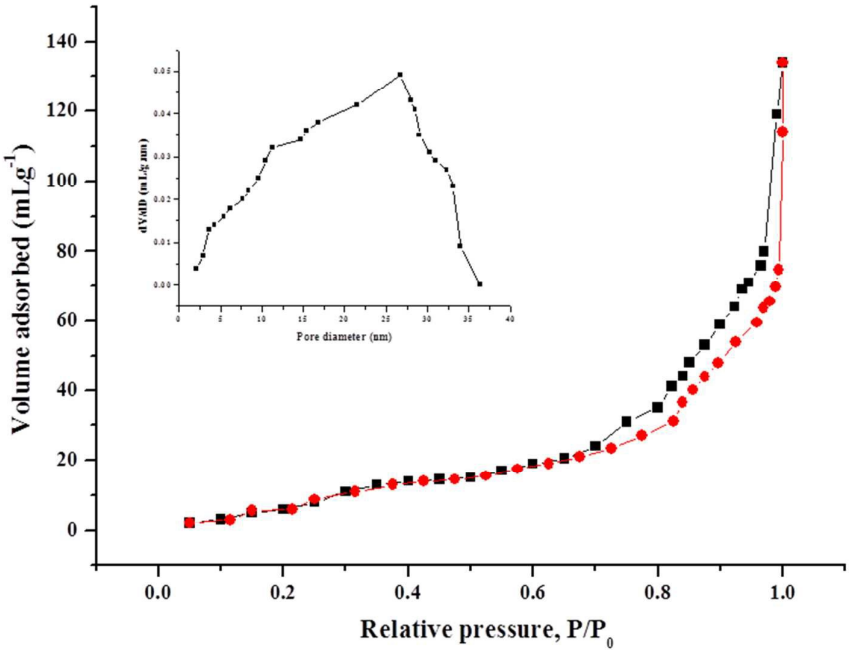


Fig.4. $N_2$ adsorption-desorption curve of the $SnO_2$-decorated $MoS_2$ nanocomposite; inset: pore diameter distribution curve

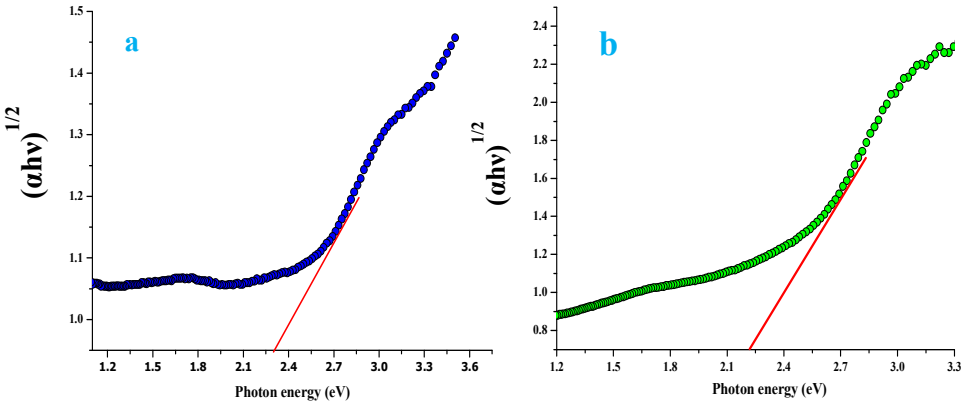


Fig.5. Tauc plots of (a) pristine $MoS_2$ and (b) $SnO_2$-decorated $MoS_2$ nanocomposite

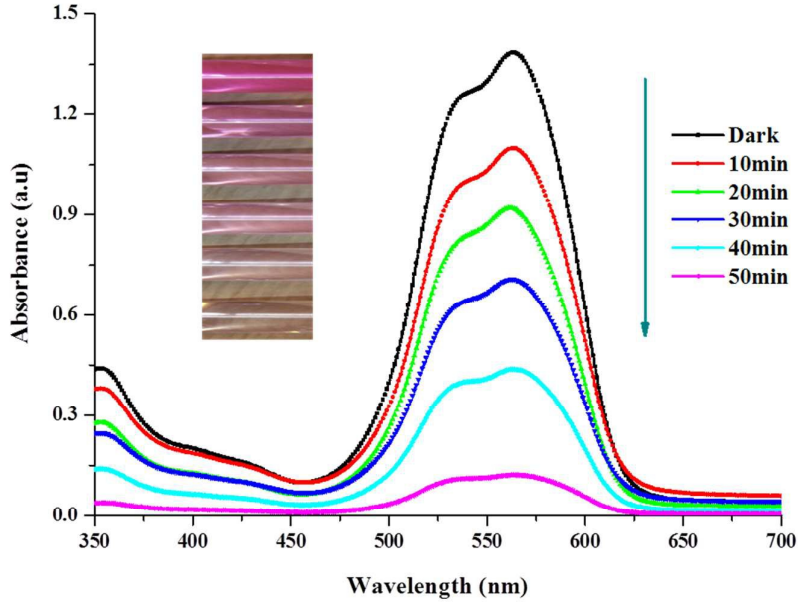


Fig.6. Time-dependent UV–vis absorbance spectra of the $SnO_2$-decorated $MoS_2$ nanocomposite

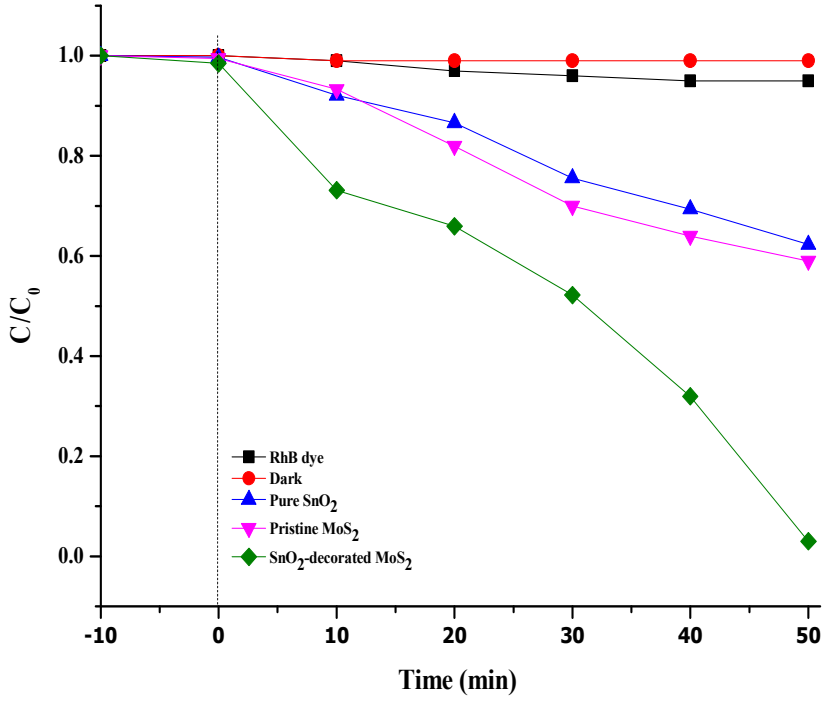


Fig.7. Photodegradation rate of the RhB pollutant under UV light and light irradiation time (50 min) of the $SnO_2$-decorated $MoS_2$ nanocomposite

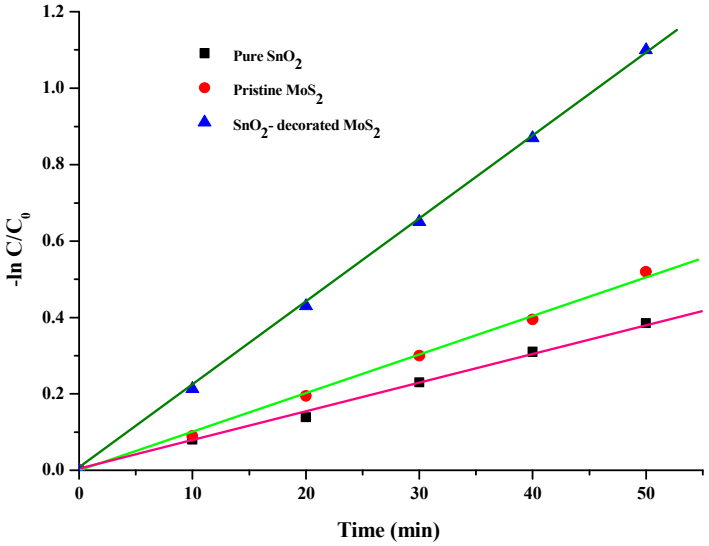


Fig.8. The kinetic plot of photocatalytic degradation of RhB with $SnO_2$-decorated $MoS_2$ nanocomposite under UV light irradiation

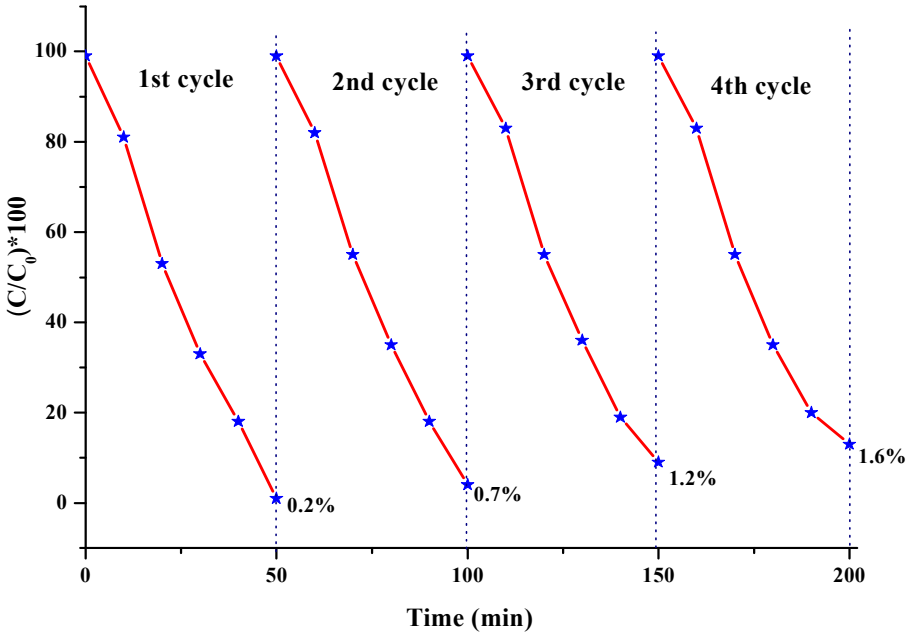


Fig.9. Recycling photocatalytic degradation of RhB in the presence of $SnO_2$-decorated $MoS_2$ nanocomposite under UV light irradiation

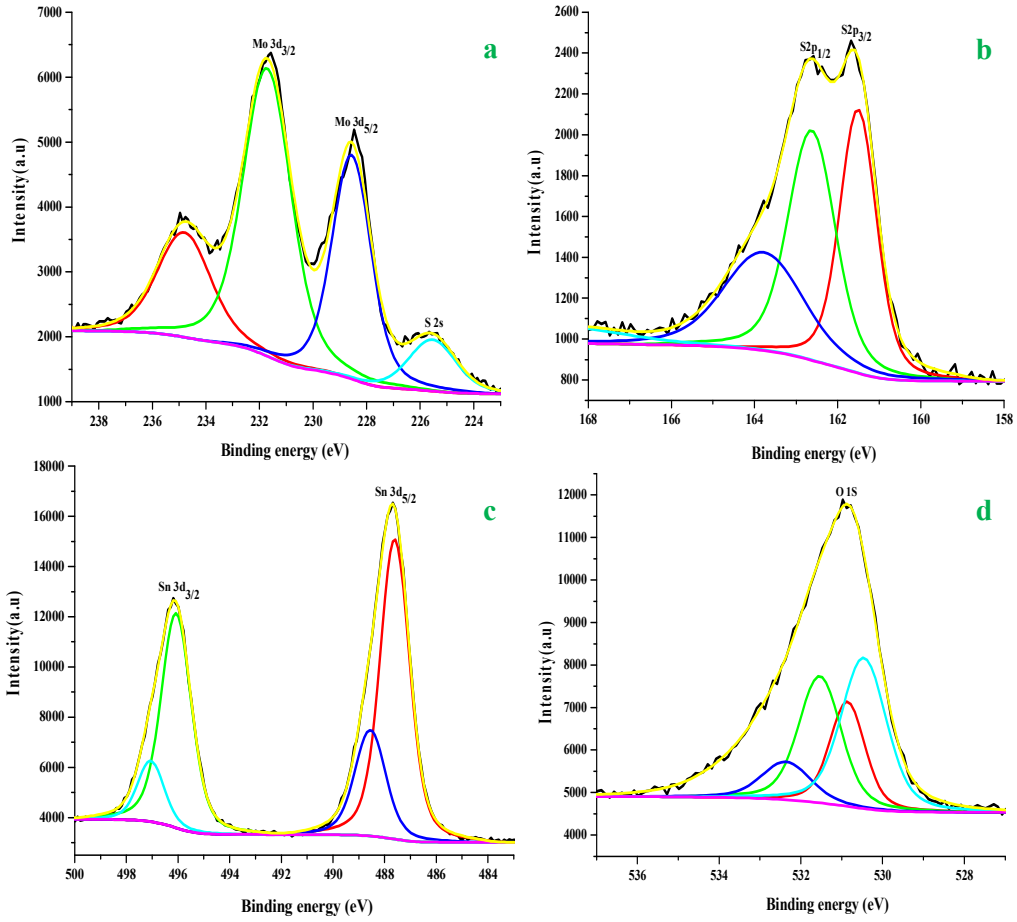


Fig.10 X-ray photoelectron spectra of $SnO_2$-decorated $MoS_2$ nanocomposite sample obtained after 4 cyclic photoreaction (a) Mo, (b) S, (c) Sn and (d) O elements

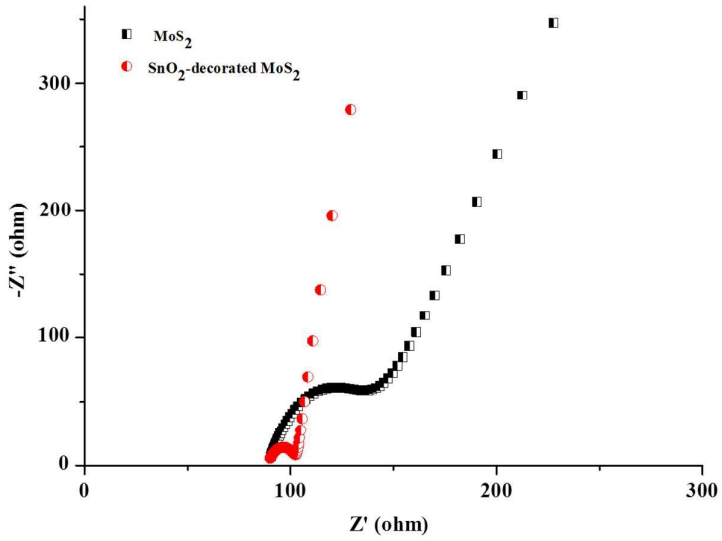


Fig.11 Electrochemical impedance spectra of pristine $MoS_2$ and $SnO_2$-decorated $MoS_2$ nanocomposite samples

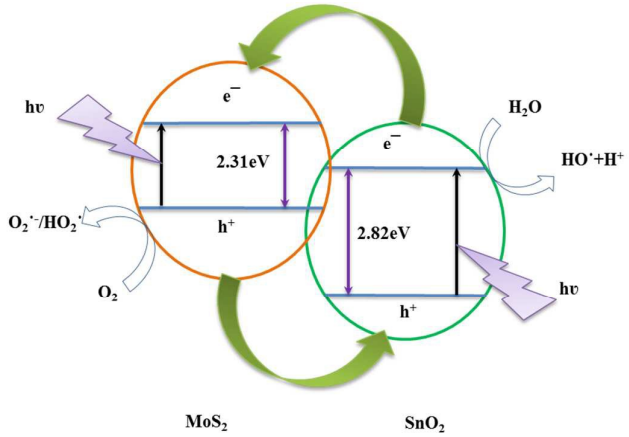


Fig.12. The proposed schematic mechanism of photogenerated electron-hole transfer process in $SnO_2$-decorated $MoS_2$ nanosheets under UV- light irradiation

Graphical Abstract